Predicting cell cycle stage from 3D single-cell nuclear-stained images

Gang Li[*1,2], Eva K. Nichols[*1], Valentino E. Browning[†1], Nicolas J. Longhi[†3], Conor Camplisson[1], Brian J. Beliveau[‡1,4], and William Stafford Noble[‡1,5]

[1]Department of Genome Sciences, University of Washington
[2]eScience Institute, University of Washington
[3]Department of Bioengineering, University of Washington
[4]Brotman Baty Institute for Precision Medicine, Seattle, WA 98195, USA
[5]Paul G. Allen School of Computer Science and Engineering, University of Washington

Abstract

The cell cycle governs the proliferation, differentiation, and regeneration of all eukaryotic cells. Profiling cell cycle dynamics is therefore central to basic and biomedical research spanning development, health, aging, and disease. However, current approaches to cell cycle profiling involve complex interventions that may confound experimental interpretation. To facilitate more efficient cell cycle annotation of microscopy data, we developed CellCycleNet, a machine learning (ML) workflow designed to simplify cell cycle staging with minimal experimenter intervention and cost. CellCycleNet accurately predicts cell cycle phase using only a fluorescent nuclear stain (DAPI) in fixed interphase cells. Using the Fucci2a cell cycle reporter system as ground truth, we collected two benchmarking image datasets and trained two ML models—a support vector machine (SVM) and a deep neural network—to classify nuclei as being in either the G1 or S/G2 phases of the cell cycle. Our results suggest that CellCycleNet outperforms state-of-the-art SVM models on each dataset individually. When trained on two image datasets simultaneously, CellCycleNet achieves the highest classification accuracy, with an improvement in AUROC of 0.08–0.09. The model also demonstrates excellent generalization across different microscopes, achieving an AUROC of 0.95. Overall, using features derived from 3D images, rather than 2D projections of those same images, significantly improves classification performance. We have released our image data, trained models, and software as a community resource.

Introduction

The cell cycle plays a crucial role in regulating the growth, differentiation, and regeneration processes of all eukaryotic cells, ensuring proper cell function and maintenance throughout the organism's life. For this reason, profiling cell cycle dynamics is central to basic and biomedical research spanning development, health, aging, and disease. For example, cell cycle staging provides insights into cellular responses to drug therapies, immune cell activity during infection, metastatic potential of tumors, tissue regeneration, cellular differentiation, and more. Current methods for cell cycle staging often depend on metabolic labeling (*e.g.*, with BrdU [35, 10]), genetic engineering (such knock-in of fluorescently tagged proteins that oscillate with the cell cycle [47, 37, 28]), DNA staining for flow cytometry [35, 2, 6, 7, 29] (propidium iodide, Hoechst, and/or DAPI), immunofluorescence against proliferative antigens [9, 16, 13, 29] (e.g., Ki67, PCNA), or directly tracking by live-cell imaging. We reasoned that a machine learning (ML) approach may simplify cell cycle staging with minimal experimenter intervention and cost. Because a nuclear counterstain, such as DAPI, is already a part of many wet lab workflows—particularly those using fixed interphase cells—we aimed to test and develop ML-based models that are capable of classifying cell cycle stage based on DAPI stained cell images alone.

[*]Equal contributions
[†]Equal contributions
[‡]Correspondence: beliveau@uw.edu, william-noble@uw.edu

Method	Year	Output	Input	Dim	# of cells	Software Avail.	Data Avail.
GMM [36]	2015	G1, S, G2/M	DAPI intensity	2D	Unclear	Commercial	Upon request
k-means [12]	2017	G1, S, G2/M	DAPI intensity and cell area	2D	10,805	No	Upon request
CNN [30]	2020	G1, S/G2	DAPI stained image	2D	3,553	No	Upon request
SVM [31]	2021	G1, S/G2	DAPI intensity and cell area	2D	3,553	Yes*	Upon request
CellCycleNet	2024	G1, S/G2	DAPI stained image	3D	7,802	Yes	Yes

Table 1: **Comparison of different cell cycle inference methods using DAPI stained nuclei.** *Code is available for the SVM but not for processing images for input to the SVM.

Many methods have previously been developed for cell cycle staging from microscopy data. These include approaches specialized for brightfield microscopy images [3, 11, 20] or live cell tracking [46, 18, 27, 22, 21, 1, 17, 37, 28, 4, 43]. We identified four similar studies to our own that focus specifically on cell cycle staging of fixed interphase cells, stained with DAPI, using fluorescence microscopy (Table 1). Of the non-ML methods, Roukos *et al.* [36] used two different methods to assign cell cycle stages to individual cells, based on three cell cycle stage bins (G1, S, and G2/M): either visually setting thresholds with respect to an empirical histogram of total DAPI intensity, or using commercial software (FCS express 5) to model the DAPI intensities with a Gaussian mixture model (GMM) [36]. Subsequently, Ferro *et al.* developed a two-dimensional k-means clustering for cell cycle classification, based on the total DAPI intensity and the cell area [12]. Of the ML methods, Narotamo *et al.* trained a support vector machine (SVM) to take into account these same two features, but they employed a two-label classification scheme (G1 versus S/G2) [31]. In separate work, the same authors also trained a type of deep learning model, a convolutional neural network (CNN), to infer cell cycle stages directly from DAPI stained images, rather than from features inferred from those images [30].

One common feature of these existing methods is that they rely on 2D data: either 2D images or 2D maximum projections of 3D images. We hypothesized that a model that makes use of 3D images would be better equipped to accurately characterize the volume and surface area of the nucleus and hence would outperform a model that relies solely on 2D information. To test this hypothesis, we gathered *in vitro* microscopy data from fixed mouse fibroblast cells. To enable accurate labeling of cell cycle stages, we used the mouse fibroblast fluorescent ubiquitination-based cell cycle indicator ("Fucci2a") cell reporter line [28]. This established Fucci2a cell line reports cell cycle stage through the fluorescent tagging of proteins that oscillate with cell cycle: hCdt1, tagged with the mCherry fluorescent protein, and hGeminin, tagged with the mVenus fluorescent protein. The relative abundance of red and green signals within a cell's nucleus is tightly correlated with the cell cycle stage. We then acquired comprehensive 3D image datasets of fixed Fucci2a cells across two common imaging modalities, epifluorescence and confocal microscopy. From these data, we trained a deep neural network model, CellCycleNet, to distinguish between nuclei in the G1 versus S/G2 phases of the cell cycle.

Our results suggest that CellCycleNet provides more accurate cell cycle classification than the current state-of-the-art ML method, the SVM of Naratamo *et al.* [31]. Our fine-tuned CellCycleNet, outperformed the SVM fitted to 2D features, achieving an area under the receiver operating characteristic curve (AUROC) of 0.95 on the epifluorescence data and 0.94 on the confocal data, representing an improvement of 8.0–9.3%. Furthermore, to verify the benefit of using 3D features, we directly compared two SVM models that rely upon the same input features: one model derives its features from 2D maximum projections whereas the other derives its features directly from 3D images. On an independent test set, we observe that the use of 3D features boosts the performance of the SVM model by 4.6–5.8%.

One challenge that this field faces is a lack of standardized benchmarks and publicly available data and/or software. Of the four references highlighted in Table 1, either the associated ground truth cell cycle labels were not readily available, the image data was not sampled enough to be truly 3D, and/or our queries to the authors were not answered. These factors prevented us from readily using currently existing image data for testing CellCycleNet. To address this problem, we make our data, software, and associated benchmarking scripts publicly available. In particular, we provide CellCycleNet as open-source software, which may be used out-of-the-box or fine-tuned as needed. CellCycleNet is implemented in Python and is available with an MIT license at `https://github.com/Noble-Lab/CellCycleNet`. We anticipate that our trained CellCycleNet model will be generally applicable in any *in vitro* setting requiring cell cycle staging, and that our benchmarking platform will be useful for future comparisons of cell cycle staging techniques.

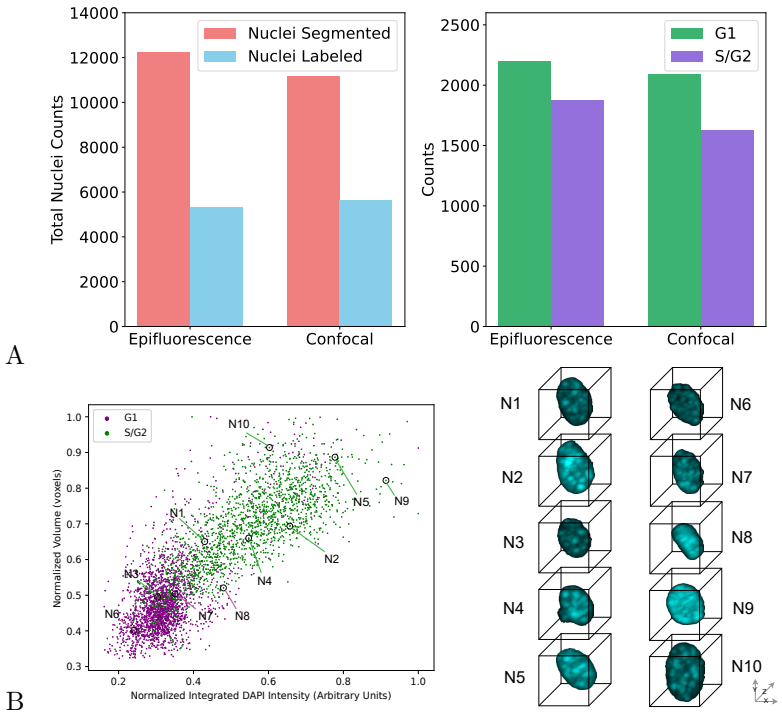

Figure 1: **A** Two benchmarking new 3D image datasets. **B** Scatter plots of confocal image datasets with top 10 representative cell images.

Results

Generating benchmark 3D image datasets from two image modalities

Widefield epifluorescence microscopy and confocal microscopy are among the most common fluorescence-based imaging modalities in laboratories. We reasoned that imaging Fucci2a cells across these two platforms would provide a comprehensive training and testing dataset for using in developing ML models. Accordingly, we collected datasets on two instruments available to us that had suitable hardware configurations for the high-throughput acquisition of the Fucci2a cells [28] at sub-cellular and sub-nuclear resolution to facilitate robust feature extraction and ground truth label assignment. As these systems have distinct optical configurations (e.g., widefield epifluorescence vs. spinning disc confocal), there were differences in the lateral and axial sampling rates used in to acquire the two datasets (see Materials and Methods). The epifluorescence dataset voxel dimensions are 188 nm in XY and 500 nm in Z. The confocal dataset voxel dimensions are 183 nm in XY and 200 nm in Z. We used Cellpose for 3D nuclear segmentation [41, 33, 40] (see Materials and Methods).

We collected in total 6,390 images of 5,331 nuclei for the epifluorescence image dataset and 93,750 images of 5,638 nuclei for the confocal image dataset. For each dataset, around 65–75% of cells exhibit Fucci signals. Following Narotamo *et al.* [31], we removed cells that had abnormal size or did not pass an RFP/GFP ratio filter. Finally, we assigned ground truth labels, following Narotamo *et al.* (2021) [31], to 4,076 cells (G1: 2,203 cells; S/G2: 1,873 cells) in the epifluorescence dataset and 3,726 cells (G1: 2,096; S/G2: 1,630) in the confocal dataset (Figure1A). Scatter plots of cells from two datasets and images of 10 representative cells (Figure1B, and Supplementary Figure S1) show that larger and brighter cells are more likely to be in S/G2. The representative cells are selected by Apricot, which uses submodular optimization to summarize large data sets into minimally redundant subsets that are representative of the original data [38].

CellCycleNet provides accurate cell cycle inference

We hypothesized that a deep neural network trained from our benchmark dataset could accurately assign cell cycle stage labels to individual cells. One lesson from the many recent successes of deep learning in various fields is that highly accurate models are often parameter-rich and trained from massive amounts of data. Although our data set is large—545 gigabytes of data—it is still small in comparison to image compendia used to train state-of-the-art image processing models. For example, ImageNet [8], a widely used dataset in image recognition, includes over 14 million images (last updated in March 2021), serving as a benchmark for training and evaluating model(s). Similarly, TissueNet [15], a dataset for segmentation models, contains over 1 million manually labeled cells, which is an order of magnitude larger than any previously published segmentation training dataset. Accordingly, we trained our model, called "CellCycleNet," using a transfer learning setup, which means that we used as a starting point a model that was previously trained from a very large collection of data to solve a related image analysis task. More specifically, we sought to fine-tune a pre-trained neural network that was designed to segment nuclei in light-sheet microscopy images [45]. The model is a 3D convolutional neural network that processes 3D images through various operations, including multiple layers of convolution and max pooling. The final output is a probability score indicating whether the input cell image belongs to the G1 phase or the S/G2 phase. The network consists of 35 layers and has a total of 1,757,267 parameters. We divided each image dataset into a 70/20/10 split for training, validation, and testing, respectively. For optimization, we employed binary cross-entropy loss and the Adam optimizer.

Our empirical analysis suggests that the trained CellCycleNet model provides more accurate cell cycle stage labels than the current state-of-the-art method, the SVM of Naratamo *et al.* [31]. Specifically, CellCycleNet achieves an area under the receiver operating characteristic curve (AUROC) of 0.94 on both the epifluorescence and the confocal data (Figure2B,C). This represents an improvement of 0.07–0.08 relative to the SVM. As an alternative performance measure, we also computed the classification accuracy at the selected decision threshold (Figure2D). By this measure, CellCycleNet also outperforms the SVM, increasing the accuracy by 7.7% on the epifluorescence dataset and 8.4% on the confocal dataset.

One challenge associated with deep neural network models is their black-box nature, which can make it difficult to understand why a particular model makes a given prediction. To address this difficulty, various saliency methods have been developed [32, 39, 42, 25], which aim to identify features of the input data that are most relevant to a given model's output. Accordingly, we applied one of the most commonly used methods, integrated gradients [42], from the Captum model interpretability library [23], to the set of 8 representative images selected by Apricot [38] (SupplementaryFigS3). The spatial patterns identified by integrated gradients suggests that CellCycleNet is focusing on DAPI bright, heterochromatic foci within the nucleus. Future investigation will be needed to determine whether the model recognizes specific organizational states of the underlying genomic regions, the high local density of the DAPI signal at these sites, or other factors.

Using 3D information improves cell cycle estimation

CellCycleNet and the SVM differ in two primary ways: first, the SVM learns from 2D whereas CellCycleNet learns from 3D images; and second, CellCycleNet uses a CNN architecture and the SVM does not. To isolate the effect of that first difference on performance, we performed an intermediate experiment, in which we trained an SVM model using features extracted from 3D images versus features extracted from 2D projections of the same images. The first SVM model, consistent with Narotamo *et al.* [31], uses two features extracted from 2D maximum-intensity projection images: 2D integrated DAPI intensity and area. The second SVM model uses two corresponding features derived from the full 3D images: 3D integrated DAPI intensity and volume.

All SVM models were implemented in Python with sklearn [34]. We found that in all cases the RBF kernel achieved the best performance. The regularization and gamma parameters were tuned on a per-model basis using nested cross-validation with sklearn's GridSearchCV object [34]. To account for differences in magnitude, all features were scaled to a mean of 0 and standard deviation of 1 using z-score normalization. Scaling features prevent a single feature from dominating the decision function, which we found to improve model performance.

Comparing the performance of the 2D and 3D SVM models on the test set images suggests the value of incorporating 3D image information. First, the SVM model integrating 3D features exhibited markedly enhanced classification performance, achieving an AUROC of 0.91 on both the confocal dataset and the

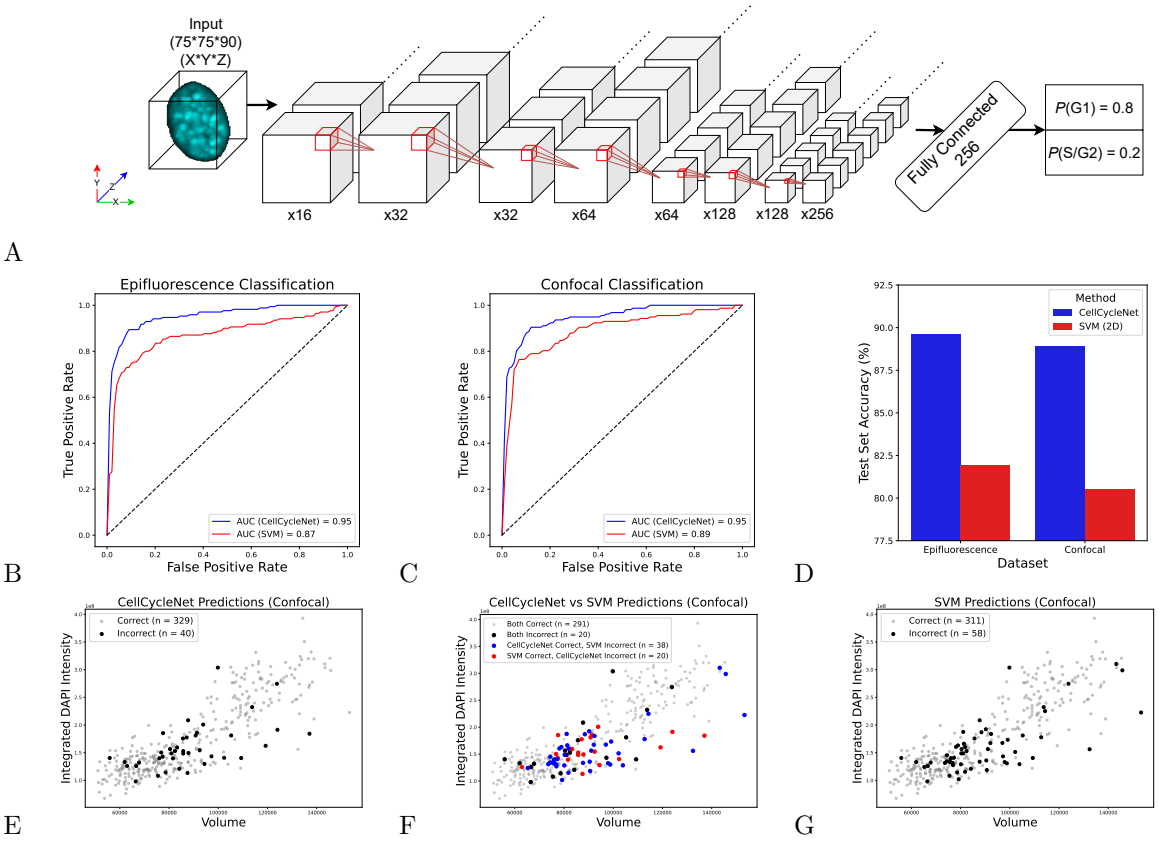

Figure 2: **CellCycleNet improves cell cycle inference on both benchmarking datasets. A** The schematics of CellCycleNet. DAPI blue intensity would be used as input, and ground truth labels are generated using hCdt1 and hGeminin. **B** ROC curves on epifluorescence data. **C** ROC curves on confocal data. **D** Bar plot of test accuracy **E** Scatter plot of CellCycleNet predictions. **F** Scatter plot of prediction differences between two models. **G** Scatter plot of SVM predictions.

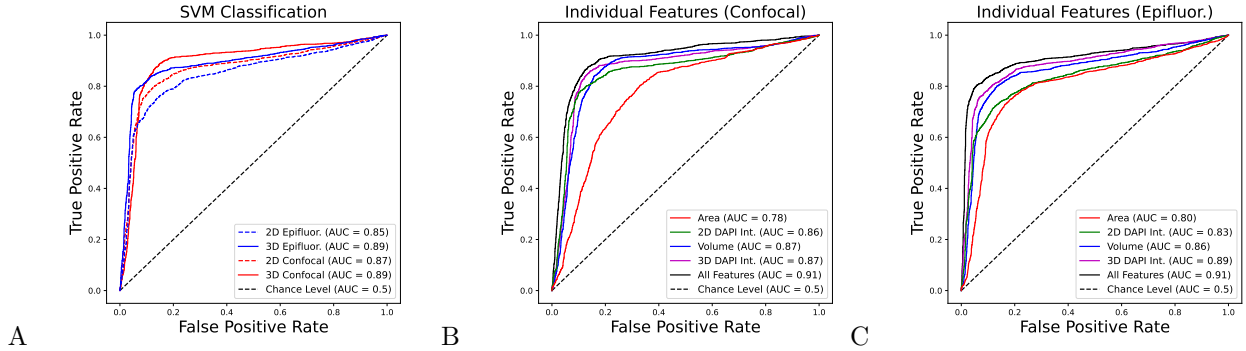

Figure 3: **Using 3D features with SVM also improves cell cycle estimation. A.** ROC curves on two image datasets using SVM models. **B.** ROC curves on confocal image dataset using each individual feature with using 4 features together with SVM. **C.** ROC curves on epifluorescence image dataset using each individual feature and with using 4 features together with SVM.

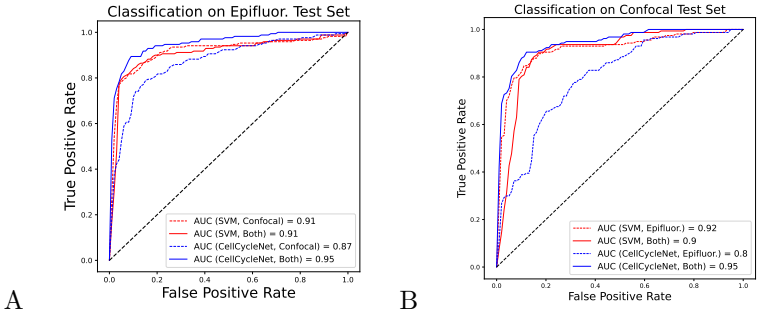

Figure 4: **CellCycleNet does not generalize well across different microscope platforms but improves once trained on both image datasets. A** ROC curves on epifluorescence test data. **B** ROC curves on confocal test data.

epifluorescence dataset (Figure 3A). These values represent a substantial increase, with the 3D model outperforming its 2D counterpart by 5.8% and 4.6% in terms of AUROC for the epifluorescence and confocal datasets, respectively. In addition, we also measured the predictive ability of each individual feature (Figure 3B–C), and we observed that 3D DAPI integrated intensity is the most predictive single feature among the four. Finally, we integrated all four features, both 2D and 3D, into a single SVM model, which yielded only a slight improvement in AUROC, from 0.91 to 0.92, compared with the 3D SVM model.

CellCycleNet's performance improves when trained on both image datasets.

After confirming that CellCycleNet accurately infers cell cycles within each image dataset, and because we acquired images from two different image modalities, we next investigated whether a model trained on data from one platform could generalize well to data from another. We evaluated CellCycleNet's generalizability in both directions: training on epifluorescence data and predicting on confocal data, and vice versa. We found that, for both directions, CellCycleNet trained on one platform performed poorly when tested on the other (Figure 4A–B).

This observation prompted us to test whether training CellCycleNet on both image datasets could match the performance of CellCycleNet trained on the two datasets independently. We found that training on both types of images resulted in the most accurate predictions, achieving an AUROC of 0.95 on both datasets (Figure 4). This performance was even better than models trained exclusively on one type of image (Figure 4A,B). In contrast, training an SVM model on the combined data set led to a decrease in performance, with an AUC decrease of 0.1–0.2, when trained on both image datasets. This observation underscores the power of the CNN to learn features intrinsic to cell cycle phasing that generalize across microscope platforms.

Discussion

We developed a machine learning model, CellCycleNet, for predicting cell cycle stages from 3D images of DAPI-stained nuclei. CellCycleNet is fine-tuned from a pre-trained 3D U-Net [45] using images from two widely used microscope modalities. This model automatically extracts critical 3D features necessary for prediction, eliminating the need for manual selection of morphological features. Our empirical evaluation of the model suggests two useful conclusions. First, incorporating 3D information into either an SVM or a deep neural network greatly improves cell cycle classification accuracy. Current state-of-the-art approaches rely on 2D max-projected image data from 3D data, which removes information between planes that contain useful features for prediction. Second, a deep neural network outperforms an SVM, particularly when trained on data from two different imaging platforms. CellCycleNet is therefore a more suitable architecture to achieve generalizability across image modalities.

CellCycleNet's current implementation does have some limitations. As with all machine learning models, users need to consider how well their data matches CellCycleNet's training data and make adjustments accordingly. For example, CellCycleNet was trained on mouse 3T3 fibroblast cells containing a Fucci2a transgene [28]. Other "workhorse" cell lines of varied shapes and sizes may be out of distribution for CellCycleNet. To address this, we provide software tools so that users with their own cell line and ground-truth labels can further fine-tune CellCycleNet to achieve more accurate cell cycle stage classification. On a related note, CellCycleNet may be sensitive to 3D segmentation performance. Because each cell line may have different nuclear shapes and sizes, users may need to adjust their segmentation methodology to achieve robust results with CellCycleNet. We encourage users to explore a variety of cell segmentation solutions, such as CellPose [41, 33, 40], Stardist [44], CellProfiler [5, 26], or others reviewed by Hollandi *et al.* [19]. Lastly, CellCycleNet currently supports only two cell cycle labels: G1 and G2/S. This limitation is due to the resolving power of the Fucci2a transgene. Ongoing efforts are improving Fucci technology to better resolve three classes (G1, S, and G2), such as with the Fucci(CA) cassette [37]. Future work can utilize these next-generation Fucci sensors for improved classification power.

Though we observed that using 3D features from images instead of 2D features was the best for improving classification performance, this does potentially cause a tradeoff for users when it comes to image data acquisition. Producing well-sampled 3D data takes more time on the microscope, which limits high-throughput data acquisition and becomes more costly. In some cases, users may opt to adopt a 2D approach that sacrifices performance and generalizability for an increased number of imaged cells and reduced cost.

We anticipate that CellCycleNet will be most useful for experimentalists who work with mouse fibroblast cells for a wide array of applications. Cell cycle progression is a key metric for evaluating cell responses to pharmacological agents, pathogenic stimuli, and in the study of gene mutations. Though there are many ways to measure cell cycle, these methods are often complex and time-consuming. In contrast, DAPI-staining of fixed cells is fast and already a part of many image analysis-based workflows. Using CellCycleNet will allow access to information from the same data "for free"—that is, with minimal to no additional hands-on experimenter effort. Additionally, because cell cycle inference uses the DAPI channel that serves as a counterstain, two or more channels are open to supporting additional targets in downstream assays, such as those provided by immunofluorescence or fluorescence *in situ* hybridization assays. Beyond technical considerations, using CellCycleNet in lieu of classic cell cycle labeling methods will be robust to side effects—both known and unknown—that can confound interpretation of experimental results. For example, BrdU pulses are inherently toxic and have been shown to increase cell death and repress differentiation in neural progenitor cells [10, 24].

We have released all our image data, trained models, and software as a community resource accessible to experimentalists. Lastly, we believe that our key finding—that 3D information significantly improves machine learning model performance—will inform future work in ML-based bioimage analysis beyond cell cycle profiling.

Materials and methods

Cell culture

The Fucci (Fluorescent Ubiquitination-based Cell Cycle Indicator) 3T3 Fucci2a reporter cell line was a gracious gift from Richard Mort [28] and maintained in complete 3T3 complete cell culture media (high glucose 4.5 g/L DMEM with 2 mM L-glutamine, 10% FBS, and 1% pen/strep antibiotic) in the presence of 100-200 ug/mL hygromycin selection antibiotic. Prior to imaging experiments, ~7x10E4 cells were seeded in a 35 mm dish. Next day, cells were fixed in 4% PFA in 1xPBS for 10 minutes, followed by three washes in 1xPBS for one minute each prior to immunofluorescence staining.

Immunofluorescence signal amplification

We performed immunofluorescence staining targeting endogenous Fucci2a mVenus and mCherry to boost signal and effectively reduce exposure time. Following cell fixation, cells were permeabilized in 1xPBS containing 0.1% Triton X-100 for ten minutes followed by three five-minute rinses in 1xPBS. Next, cells were blocked with BlockAid Blocking Solution (Thermo, cat. no. B10710) containing 0.05% Tween-20 for thirty minutes at room temperature. Cells were then stained with a primary antibody solution overnight at 4C: 3% BlockAid Blocking Solution in 1xPBS with 1:100 concentration of both primary goat anti GFP (Encor Biotechnologies, cat. No. GPCA-GFP) and rabbit anti RFP (Rockland, cat. No. 600-401-379) antibodies. After three five-minute rinses in 1xPBS, cells underwent secondary antibody staining for 30 minutes with the following solution: 1:1000 concentration of donkey anti goat AF488 (Thermo, cat. No. A32814) and donkey anti rabbit AF555 (Thermo, cat. no. A32794) and 143 µM DAPI (Thermo, cat. no. D1306) in 1xPBS. After, cells underwent three five-minute rinses in 1xPBS before covered in SlowFade Gold Antifade Mountant (Thermo, cat. no. S36936). Stained cells were stored in the dark at 4C until image data acquisition.

Epifluorescence dataset acquisition

The epifluorescence image dataset was acquired using a Keyence BZ-X800 fluorescence microscope. All images were acquired using the Keyence Plan Apochromatic 40x objective lens (model PZ-PA40, PlanApo NA 0.95/0.17 mm default). A tiled acquisition was obtained over approximately 5 mm2 of the cell culture plate, at fixed z range of 35 µm, z-step of 0.5 µm, and optical sectioning width of 10. 100% excitation light (metal halide lamp) was used with no binning and monochromatic camera with a digital zoom of x1.0. Each image consists of three fluorescent channels: nuclear stain DAPI (using the DAPI filter cube; model OP-87762, 360/40 nm excitation filter, 400 nm longpass dichroic mirror, 460/50 nm emission filter; 1/1.2s exposure time), the mVenus-hGeminin-AF488 signal (via the GFP filter cube; model OP-87763, excitation wavelength 470/40 nm, emission wavelength 525/50 nm, dichroic mirror wavelength 495 nm; 1/2.3s exposure time), and the mCherry-hCdt1-AF555 signal (via the Cy3/TRITC filter cube; CHROMA model 49004, excitation wavelength 545/25 nm, emission wavelength 605/70 nm, dichroic mirror wavelength 565 nm; 1/7.5s exposure time). An integrated CCD camera was used in 14-bit mode, without binning and with a physical pixel size of 7.549 µm, resulting in an effective pixel size of 188.7 nm while imaging at 40x magnification. The final dataset used for analysis and model training consists of 19,170 total images over 90 tiled z-stacks (71 images per z-stack) and 3 channels; each image is 1440x1920 pixels. The voxel size for each image in the dataset was 188nm*188nm *500nm (X*Y*Z).

Confocal dataset acquisition

The confocal image dataset was acquired using a Nikon Ti2 inverted fluorescence microscope with a Yokogawa CSU W-1 SoRa spinning disk unit. A tiled acquisition was obtained over approximately 21 mm2 of the cell culture plate, at fixed z range of 30 µm and z-step of 0.2 µm. Each image consists of three fluorescent channels, using excitation light emitted at 30 percent maximal intensity from 405 nm, 488 nm, and 561 nm lasers housed in a Nikon LUNF 405/488/561/640NM 1F commercial launch. The nuclear stain DAPI was excited by the 405 nm laser line at 300 ms exposure; the mVenus-hGeminin-AF488 signal was excited by the 488 nm laser line at 300 ms exposure; the mCherry-hCdt1-AF555 signal was excited by the 561 nm laser line at 300 ms exposure. Laser excitation was conveyed through a single-mode optical fiber fed into the CSU-W1

SoRa unit and directed through a microlens array and 'SoRa' disc containing 50 µm pinholes. A Nikon Plan Apochromat Lambda 60X air objective lens (NA 0.95/0.17 mm) was used to project the excitation and collects the emission light. Emission light was relayed by a 1x lens, through the pinhole disc, after which it was spectrally separated by a quad bandpass dichroic mirror (Semrock Di01-T405/488/568/647-13x15x0.5) and then filtered by one of three single bandpass filters (DAPI: Chroma ET455/50M; mVenus-hGeminin-AF488: Chroma ET525/36M; mCherry-hCdt1-AF555:Chroma ET605/50M). Emission light was then focused by a 1x relay lens onto an Andor Sona 4.2B-11 camera with a physical pixel size of 11 µm, resulting in an effective pixel size of 110 nm. The Andor Sona 4.2B-11 camera was operated in 16-bit mode with rolling shutter. The final dataset used for analysis and model training consists of 625 tiled z-stacks (150 images per z-stack) and 3 channels; each image is 1024x1024 pixels. The voxel size for each image in the dataset was 182nm*182nm*200nm (X*Y*Z).

3D Segmentation

To quantify features of single nuclei, we performed 3D instance segmentation with Cellpose [41]. Specifically, for the epifluorescence dataset, we used Cellpose 2.0 out-of-the-box using the "CP" model [41, 33]. For the confocal dataset, we used the Cellpose 3.0 package with human-in-the-loop finetuning of the "cyto3" model [40]. For each tile in our dataset, we extract the nuclear channel (stained with DAPI) and downsample the image by a factor of 2 in the X and Y dimensions. We found that downsampling improves the segmentation results when using Cellpose's pre-trained models with no fine-tuning. We removed poor segmentation by ignoring objects contacting the image boundary and segmentation with a solidity (ratio of convex hull to total mask volume) of < 0.9.

Image preprocessing

We implemented several preprocessing steps and applied them to the imaging data before creating the training/validation/testing datasets. First, we used the 3D instance segmentation mask to generate single-nucleus images centered on the nucleus' centroid and padded to a size of 150px*150px*90 (X*Y*Z). Next, each image in the epifluorescence dataset was downsampled by a factor of 2 in the X and Y dimensions to mitigate the data's anisotropy. Confocal images were downsampled by a factor of 2 in the X, Y, and Z dimensions to more closely match the isotropic voxel size of the efflorescence images. Then, each image was normalized independently using mean normalization. To achieve this, we first calculated the median values of all nonzero pixels for each image in the training dataset. The validation and test datasets were then normalized by dividing the pixel values of each image by the median of medians of images in the training dataset. The final preprocessed images for both datasets were then padded to a shape of 75px*75px*90 (X*Y*Z).

Data split and augmentation

After each image was preprocessed, we generated the training/validation/testing datasets using a 70%/20%/10% split for each dataset, respectively. We used a fixed random seed during splitting to ensure consistency across different training/evaluation sessions. Data augmentation was used to expand the training set and improve model generalization. Specifically, a random rotation in the range (0°,359°) about the Z axis was applied with equal probability.

Quantification of nuclear features

Each image in the dataset was processed using an analysis pipeline developed in Python. First, each Z-series for each channel in a given tile of the dataset is loaded into memory as a 3-dimensional numpy array with the Python package tiffile [14]. All images consisting of overlap from the image tiling procedure were cropped to ensure there were no duplicate objects. To extract features of interest from the data, we performed 3D instance segmentation on the DAPI channel (as described above) [41] to generate masks corresponding to individual nuclei. Each segmentation mask was filtered to remove low-quality segmentation results. Specifically, we removed partial segmentations which contacted the image border, and removed objects

considered doublets. To quantify segmentation doublets, we calculated the concavity of the object using the regionprops() function from skimage, and removed objects with a value < 0.9 of the 'solidity' property. We then used the filtered segmentation mask to quantify features of interest from each segmented nucleus, and store the features in a pandas DataFrame. Features that were calculated are as follows: aggregate volumetric fluorescent intensity in each channel, nuclear volume, lengths of the major and minor axes of each nucleus, and metadata for each object such as the parent tile and object ID. We then stored images of each object's 405/DAPI channel, cropped to a standardized 75px*75px*90 (X*Y*Z) volume.

Cell cycle ground truth

Ground truth labels (G1 or S/G2) were generated with reference to the methodology described by Narotamo, *et al.* [31]. Prior to assigning labels, each segmented object was passed through several filters to remove nuclei that did not express the Fucci2a fluorescent proteins, had abnormal sizes, or were transitioning between cell cycle phases. Objects were excluded from our analysis if they met any of the following criteria, where R = mCherry-hCdt1 intensity, G = mVenus-hGeminin intensity, V = number of voxels in segmentation mask, and μ and σ are the mean and standard deviation of each variable, respectively. Values for μ_R and μ_G were normalized before the ratio filter was applied to account for differences in fluorescent intensity distributions between channels.

Low-Intensity Filter:
$\mu_R < 1,500$ or $\mu_G < 2,200$ (Epifluorescence)
$\mu_R < 700$ or $\mu_G < 2,000$ (Confocal)

Ratio Filter:
$0.9 < \mu_G/\mu_R < 1.1$

Volume Filter:
$|V - \mu_V| > 2.5\sigma_V$

Of the 5,331 segmented objects in the epifluorescence dataset, 1,255 met one of the above criteria and were filtered out. The remaining 4,076 objects were labeled as G1 if $R > G$ or S/G2 if $R < G$, resulting in 2,203 objects labeled G1 and 1,873 objects labeled S/G2. Of the 5,638 segmented objects in the confocal dataset, 1,912 met one of the above criteria and were filtered out. Labels were assigned to the remaining 3,726 objects with the previously described method, resulting in 2,096 objects labeled G1 and 1,630 objects labeled S/G2. In both datasets, the majority of filtered objects were excluded due to low fluorescent protein signals.

CellCycleNet

CellCycle is based on a 3D convolutional neural network (`https://github.com/wolny/pytorch-3dunet`) that was trained to perform semantic segmentation of nuclei in lightsheet images [45]. To retool this model for binary classification, we used the first four convolutional blocks for feature extraction, and we appended four additional layers in total to perform the classification task: one 3DAdaptiveMaxPooling layer with an output size of (1,1,1), one Flatten layer with $start\_dim = 1$, one Dropout layer with probability 0.5, and one Linear layer with 256 input features and 1 output features. The resulting model contains 35 layers and a total of 1,757,267 parameters. CellCycleNet is trained using binary cross-entropy as the loss function, and each model is trained for 800 epochs, with the checkpoint showing the highest validation accuracy being selected. All models were trained using a batch size of 4, Adam optimizer with an initial learning rate of 1e-5 and weight decay of 1e-1.

Software and data availability

We developed an image processing pipeline with the goal of training an image classification model capable of predicting the cell cycle state from a volumetric imaging dataset of the Fucci2a cells, cultured and fixed in 35mm plates. All code was developed in Python using the Anaconda package manager to create a

standardized analysis environment. Our CellCycleNet is available at `https://github.com/Noble-Lab/CellCycleNet`.

The raw and segmented image data have been submitted for review at the Image Data Resource (`https://idr.openmicroscopy.org`).

Acknowledgments

We thank Dr. Richard Mort and Dr. Jennifer Kong for their gracious gift of the Fucci2a knock-in cell line and 3T3 fibroblast parental cell line, respectively. E.K.N thanks all faculty at the Deep Learning for Microscopy Image Analysis Course (2023) at the MBL for their excellent instruction. We thank members of the Noble, Beliveau, and Shendure labs for helpful discussion.

Funding

This work is supported by NIH award UM1 HG011531. E.K.N is supported by the Washington Research Foundation Postdoctoral Fellowship. G.L.'s research is supported by University of Washington eScience Institute.

Author contributions

G.L.: Conceptualization, Methodology, Formal analysis, Investigation, Supervision, Writing—Original Draft, Reviewing and Editing. E.K.N.: Data curation, Conceptualization, Investigation, Supervision, Writing—Original Draft, Reviewing and Editing. V.E.B.: Data Curation, Visualization, Methodology, Formal analysis, Investigation, Writing—Review and Editing. N.J.L.: Data Curation, Formal analysis, Visualization, Software, Investigation, Writing—Review and Editing. C.C.: Software. B.J.B. and W.N.: Supervision, Funding acquisition, Writing—Reviewing and Editing.

References

[1] S. Acharya, A. Ganguly, R. Sarkar, and A. Jose. Cell Cycle State Prediction Using Graph Neural Networks, Feb. 2024. Pages: 2024.01.30.577893 Section: New Results.

[2] F. Belloc, P. Dumain, M. R. Boisseau, C. Jalloustre, J. Reiffers, P. Bernard, and F. Lacombe. A flow cytometric method using Hoechst 33342 and propidium iodide for simultaneous cell cycle analysis and apoptosis determination in unfixed cells. *Cytometry*, 17(1):59–65, 1994. _eprint: https://onlinelibrary.wiley.com/doi/pdf/10.1002/cyto.990170108.

[3] T. Blasi, H. Hennig, H. D. Summers, F. J. Theis, J. Cerveira, J. O. Patterson, D. Davies, A. Filby, A. E. Carpenter, and P. Rees. Label-free cell cycle analysis for high-throughput imaging flow cytometry. *Nature Communications*, 7(1):10256, Jan. 2016. Publisher: Nature Publishing Group.

[4] J. M. Campbell, A. Habibalahi, S. Mahbub, M. Gosnell, A. G. Anwer, S. Paton, S. Gronthos, and E. Goldys. Non-destructive, label free identification of cell cycle phase in cancer cells by multispectral microscopy of autofluorescence. *BMC Cancer*, 19(1):1242, Dec. 2019.

[5] A. E. Carpenter, T. R. Jones, M. R. Lamprecht, C. Clarke, I. H. Kang, O. Friman, D. A. Guertin, J. H. Chang, R. A. Lindquist, J. Moffat, P. Golland, and D. M. Sabatini. CellProfiler: image analysis software for identifying and quantifying cell phenotypes. *Genome Biology*, 7(10):R100, Oct. 2006.

[6] M. J. Cecchini, M. Amiri, and F. A. Dick. Analysis of cell cycle position in mammalian cells. *JoVE (Journal of Visualized Experiments)*, (59):e3491, 2012.

[7] Z. Darzynkiewicz, G. Juan, and E. Bedner. Determining Cell Cycle Stages by Flow Cytometry. *Current Protocols in Cell Biology*, 1(1):8.4.1–8.4.18, 1999. _eprint: https://onlinelibrary.wiley.com/doi/pdf/10.1002/0471143030.cb0804s01.

[8] J. Deng, W. Dong, R. Socher, L.-J. Li, K. Li, and L. Fei-Fei. ImageNet: A large-scale hierarchical image database. In *2009 IEEE Conference on Computer Vision and Pattern Recognition*, pages 248–255, June 2009. ISSN: 1063-6919.

[9] D. R. Dietrich. Toxicological and Pathological Applications of Proliferating Cell Nuclear Antigen (PCNA), A Novel Endogenous Marker for Cell Proliferation. *Critical Reviews in Toxicology*, 23(1):77–109, Jan. 1993. Publisher: Taylor & Francis _eprint: https://doi.org/10.3109/10408449309104075.

[10] A. Duque and P. Rakic. Identification of Proliferating and Migrating Cells by BrdU and Other Thymidine Analogs: Benefits and Limitations. In A. Merighi and L. Lossi, editors, *Immunocytochemistry and Related Techniques*, pages 123–139. Springer, New York, NY, 2015.

[11] P. Eulenberg, N. Köhler, T. Blasi, A. Filby, A. E. Carpenter, P. Rees, F. J. Theis, and F. A. Wolf. Reconstructing cell cycle and disease progression using deep learning. *Nature Communications*, 8(1):463, Sept. 2017. Publisher: Nature Publishing Group.

[12] A. Ferro, T. Mestre, P. Carneiro, I. Sahumbaiev, R. Seruca, and J. M. Sanches. Blue intensity matters for cell cycle profiling in fluorescence DAPI-stained images. *Laboratory Investigation*, 97(5):615–625, May 2017.

[13] J. Gerdes, H. Lemke, H. Baisch, H. H. Wacker, U. Schwab, and H. Stein. Cell cycle analysis of a cell proliferation-associated human nuclear antigen defined by the monoclonal antibody Ki-67. *The Journal of Immunology*, 133(4):1710–1715, Oct. 1984.

[14] C. Gohlke. cgohlke/tifffile: v2022.5.4, 2022.

[15] N. F. Greenwald, G. Miller, E. Moen, A. Kong, A. Kagel, T. Dougherty, C. C. Fullaway, B. J. McIntosh, K. X. Leow, M. S. Schwartz, C. Pavelchek, S. Cui, I. Camplisson, O. Bar-Tal, J. Singh, M. Fong, G. Chaudhry, Z. Abraham, J. Moseley, S. Warshawsky, E. Soon, S. Greenbaum, T. Risom, T. Hollmann, S. C. Bendall, L. Keren, W. Graf, M. Angelo, and D. Van Valen. Whole-cell segmentation of tissue images with human-level performance using large-scale data annotation and deep learning. *Nature Biotechnology*, 40(4):555–565, Apr. 2022. Publisher: Nature Publishing Group.

[16] P. A. Hall, D. A. Levison, A. L. Woods, C. C.-W. Yu, D. B. Kellock, J. A. Watkins, D. M. Barnes, C. E. Gillett, R. Camplejohn, R. Dover, N. H. Waseem, and D. P. Lane. Proliferating cell nuclear antigen (PCNA) immunolocalization in paraffin sections: An index of cell proliferation with evidence of deregulated expression in some, neoplasms. *The Journal of Pathology*, 162(4):285–294, 1990. _eprint: https://onlinelibrary.wiley.com/doi/pdf/10.1002/path.1711620403.

[17] Y. R. He, S. He, M. E. Kandel, Y. J. Lee, C. Hu, N. Sobh, M. A. Anastasio, and G. Popescu. Cell Cycle Stage Classification Using Phase Imaging with Computational Specificity. *ACS Photonics*, 9(4):1264–1273, Apr. 2022. Publisher: American Chemical Society.

[18] M. Held, M. H. A. Schmitz, B. Fischer, T. Walter, B. Neumann, M. H. Olma, M. Peter, J. Ellenberg, and D. W. Gerlich. CellCognition: time-resolved phenotype annotation in high-throughput live cell imaging. *Nature Methods*, 7(9):747–754, Sept. 2010. Publisher: Nature Publishing Group.

[19] R. Hollandi, N. Moshkov, L. Paavolainen, E. Tasnadi, F. Piccinini, and P. Horvath. Nucleus segmentation: towards automated solutions. *Trends in Cell Biology*, 32(4):295–310, Apr. 2022. Publisher: Elsevier.

[20] X. Jin, Y. Zou, and Z. Huang. An Imbalanced Image Classification Method for the Cell Cycle Phase. *Information*, 12(6):249, June 2021. Number: 6 Publisher: Multidisciplinary Digital Publishing Institute.

[21] A. Jose, R. Roy, D. Eschweiler, I. Laube, R. Azad, D. Moreno-Andrés, and J. Stegmaier. End-to-End Classification of Cell-Cycle Stages with Center-Cell Focus Tracker Using Recurrent Neural Networks. In *ICASSP 2023 - 2023 IEEE International Conference on Acoustics, Speech and Signal Processing (ICASSP)*, pages 1–5, June 2023. ISSN: 2379-190X.

[22] A. Jose, R. Roy, D. Moreno-Andrés, and J. Stegmaier. Automatic detection of cell-cycle stages using recurrent neural networks. *PLOS ONE*, 19(3):e0297356, Mar. 2024. Publisher: Public Library of Science.

[23] N. Kokhlikyan, V. Miglani, M. Martin, E. Wang, B. Alsallakh, J. Reynolds, A. Melnikov, N. Kliushkina, C. Araya, S. Yan, and O. Reblitz-Richardson. Captum: A unified and generic model interpretability library for PyTorch, Sept. 2020. arXiv:2009.07896 [cs, stat].

[24] B. Lehner, B. Sandner, J. Marschallinger, C. Lehner, T. Furtner, S. Couillard-Despres, F. J. Rivera, G. Brockhoff, H.-C. Bauer, N. Weidner, and L. Aigner. The dark side of BrdU in neural stem cell biology: detrimental effects on cell cycle, differentiation and survival. *Cell and Tissue Research*, 345(3):313–328, Sept. 2011.

[25] S. M. Lundberg and S.-I. Lee. A Unified Approach to Interpreting Model Predictions. In *Advances in Neural Information Processing Systems*, volume 30. Curran Associates, Inc., 2017.

[26] C. McQuin, A. Goodman, V. Chernyshev, L. Kamentsky, B. A. Cimini, K. W. Karhohs, M. Doan, L. Ding, S. M. Rafelski, D. Thirstrup, W. Wiegraebe, S. Singh, T. Becker, J. C. Caicedo, and A. E. Carpenter. CellProfiler 3.0: Next-generation image processing for biology. *PLOS Biology*, 16(7):e2005970, July 2018. Publisher: Public Library of Science.

[27] D. Moreno-Andrés, A. Bhattacharyya, A. Scheufen, and J. Stegmaier. LiveCellMiner: A new tool to analyze mitotic progression. *PLOS ONE*, 17(7):e0270923, July 2022. Publisher: Public Library of Science.

[28] R. L. Mort, M. J. Ford, A. Sakaue-Sawano, N. O. Lindstrom, A. Casadio, A. T. Douglas, M. A. Keighren, P. Hohenstein, A. Miyawaki, and I. J. Jackson. Fucci2a: A bicistronic cell cycle reporter that allows Cre mediated tissue specific expression in mice. *Cell Cycle*, 13(17):2681–2696, Sept. 2014. Publisher: Taylor & Francis _eprint: https://doi.org/10.4161/15384101.2015.945381.

[29] L. Muskhelishvili, J. R. Latendresse, R. L. Kodell, and E. B. Henderson. Evaluation of Cell Proliferation in Rat Tissues with BrdU, PCNA, Ki-67(MIB-5) Immunohistochemistry and In Situ Hybridization for Histone mRNA. *Journal of Histochemistry & Cytochemistry*, 51(12):1681–1688, Dec. 2003. Publisher: Journal of Histochemistry & Cytochemistry.

[30] H. Narotamo, M. S. Fernandes, J. Miguel Sanches, and M. Silveira. Interphase Cell Cycle Staging using Deep Learning. In *2020 42nd Annual International Conference of the IEEE Engineering in Medicine & Biology Society (EMBC)*, pages 1432–1435, July 2020. ISSN: 2694-0604.

[31] H. Narotamo, M. S. Fernandes, A. M. Moreira, S. Melo, R. Seruca, M. Silveira, and J. M. Sanches. A machine learning approach for single cell interphase cell cycle staging. *Scientific Reports*, 11(1):19278, Sept. 2021. Publisher: Nature Publishing Group.

[32] L. Nieradzik, H. Stephani, J. Sieburg-Rockel, S. Helmling, A. Olbrich, and J. Keuper. Challenging the Black Box: A Comprehensive Evaluation of Attribution Maps of CNN Applications in Agriculture and Forestry, Feb. 2024. arXiv:2402.11670 [cs].

[33] M. Pachitariu and C. Stringer. Cellpose 2.0: how to train your own model. *Nature Methods*, 19(12):1634–1641, Dec. 2022. Publisher: Nature Publishing Group.

[34] F. Pedregosa, G. Varoquaux, A. Gramfort, V. Michel, B. Thirion, O. Grisel, M. Blondel, P. Prettenhofer, R. Weiss, V. Dubourg, J. Vanderplas, A. Passos, and D. Cournapeau. Scikit-learn: Machine Learning in Python. *MACHINE LEARNING IN PYTHON*, 2011.

[35] P. S. Rabinovitch, M. Kubbies, Y. C. Chen, D. Schindler, and H. Hoehn. BrdU—Hoechst flow cytometry: A unique tool for quantitative cell cycle analysis. *Experimental Cell Research*, 174(2):309–318, Feb. 1988.

[36] V. Roukos, G. Pegoraro, T. C. Voss, and T. Misteli. Cell cycle staging of individual cells by fluorescence microscopy. *Nature Protocols*, 10(2):334–348, Feb. 2015. Publisher: Nature Publishing Group.

[37] A. Sakaue-Sawano, M. Yo, N. Komatsu, T. Hiratsuka, T. Kogure, T. Hoshida, N. Goshima, M. Matsuda, H. Miyoshi, and A. Miyawaki. Genetically Encoded Tools for Optical Dissection of the Mammalian Cell Cycle. *Molecular Cell*, 68(3):626–640.e5, Nov. 2017.

[38] J. Schreiber, J. Bilmes, and W. S. Noble. apricot: Submodular selection for data summarization in Python. *Journal of Machine Learning Research*, 21(161):1–6, 2020.

[39] R. R. Selvaraju, M. Cogswell, A. Das, R. Vedantam, D. Parikh, and D. Batra. Grad-CAM: Visual Explanations from Deep Networks via Gradient-Based Localization. *International Journal of Computer Vision*, 128(2):336–359, Feb. 2020.

[40] C. Stringer and M. Pachitariu. Cellpose3: one-click image restoration for improved cellular segmentation, Feb. 2024. Pages: 2024.02.10.579780 Section: New Results.

[41] C. Stringer, T. Wang, M. Michaelos, and M. Pachitariu. Cellpose: a generalist algorithm for cellular segmentation. *Nature Methods*, 18(1):100–106, Jan. 2021. Publisher: Nature Publishing Group.

[42] M. Sundararajan, A. Taly, and Q. Yan. Axiomatic Attribution for Deep Networks. In *Proceedings of the 34th International Conference on Machine Learning*, pages 3319–3328. PMLR, July 2017. ISSN: 2640-3498.

[43] K. Ulicna, M. Kelkar, C. J. Soelistyo, G. T. Charras, and A. R. Lowe. Learning dynamic image representations for self-supervised cell cycle annotation, May 2023. Pages: 2023.05.30.542796 Section: New Results.

[44] M. Weigert, U. Schmidt, R. Haase, K. Sugawara, and G. Myers. Star-convex Polyhedra for 3D Object Detection and Segmentation in Microscopy. In *2020 IEEE Winter Conference on Applications of Computer Vision (WACV)*, pages 3655–3662, Snowmass Village, CO, USA, Mar. 2020. IEEE.

[45] A. Wolny, L. Cerrone, A. Vijayan, R. Tofanelli, A. V. Barro, M. Louveaux, C. Wenzl, S. Strauss, D. Wilson-Sánchez, R. Lymbouridou, S. S. Steigleder, C. Pape, A. Bailoni, S. Duran-Nebreda, G. W. Bassel, J. U. Lohmann, M. Tsiantis, F. A. Hamprecht, K. Schneitz, A. Maizel, and A. Kreshuk. Accurate and versatile 3D segmentation of plant tissues at cellular resolution. *eLife*, 9:e57613, July 2020. Publisher: eLife Sciences Publications, Ltd.

[46] Q. Zhong, A. G. Busetto, J. P. Fededa, J. M. Buhmann, and D. W. Gerlich. Unsupervised modeling of cell morphology dynamics for time-lapse microscopy. *Nature Methods*, 9(7):711–713, July 2012. Publisher: Nature Publishing Group.

[47] N. Zielke and B. A. Edgar. FUCCI sensors: powerful new tools for analysis of cell proliferation. *WIREs Developmental Biology*, 4(5):469–487, 2015. _eprint: https://onlinelibrary.wiley.com/doi/pdf/10.1002/wdev.189.